



High-Pressure Behavior of Ferromagnesite ($\text{Mg}_{0.81}\text{Fe}_{0.19}$) CO_3 by Synchrotron X-Ray Diffraction and Raman Spectroscopy up to 53 GPa

Lin Liang¹, Guibin Zhang¹, Shengxuan Huang¹, Jingjing Niu², Dongzhou Zhang³, Jingui Xu³,
Wen Liang⁴, Shan Qin^{1*}

1. Key Laboratory of Orogenic Belts and Crustal Evolution, MOE, and School of Earth and Space Sciences, Peking University, Beijing 100871, China
2. CAS Center of Excellence in Tibetan Plateau Earth Sciences and Key Laboratory of Continental Collision and Plateau Uplift, Institute of Tibetan Plateau Research, Chinese Academy of Sciences, Beijing 100101, China
3. Hawai'i Institute of Geophysics and Planetology, School of Ocean and Earth Science and Technology, University of Hawai'i at Manoa, Hawai'i 96822, U.S.A.
4. Key Laboratory of High Temperature and High Pressure Study of the Earth's Interior, Institute of Geochemistry, Chinese Academy of Sciences, Guiyang 550081, China

 Lin Liang: <https://orcid.org/0000-0003-1569-4300>;  Shan Qin: <https://orcid.org/0000-0001-7327-1264>

ABSTRACT: Ferromagnesite (Mg, Fe) CO_3 with 20 mol% iron is a potential host mineral for carbon transport and storage in the Earth mantle. The high-pressure behavior of synthetic ferromagnesite ($\text{Mg}_{0.81}\text{Fe}_{0.19}$) CO_3 up to 53 GPa was investigated by synchrotron X-ray diffraction (XRD) and Raman spectroscopy. The iron bearing carbonate underwent spin transition at around 44–46 GPa accompanied by a volume collapse of 1.8%, which also demonstrated a variation in the dv/dP slope of the Raman modes. The pressure-volume data was fitted by a third-order Birch-Murnaghan equation of state (BM-EoS) for the high spin phase. The best-fit $K_0 = 108(1)$ GPa and $K'_0 = 4.2(1)$. Combining the dv/dP and the K_0 , the mode Grüneisen parameters of each vibrational mode (T , L , v_4 and v_1) were calculated. The effects of iron concentration on the $\text{Mg}_{1-x}\text{Fe}_x\text{CO}_3$ system related to high-pressure compressibility and vibrational properties are discussed. These results expand the knowledge of the physical properties of carbonates and provide insights to the potential deep carbon host.

KEY WORDS: ferromagnesite, synchrotron XRD, Raman spectroscopy, high pressure, geochemistry, mineral.

0 INTRODUCTION

The construction of the mineralogical models through the properties of mantle minerals is essential to understand the seismological, thermal and compositional characteristics of the deep Earth. Carbonates in the mantle have an evident effect on the physical and chemical properties of the Earth's interior, such as melting, elasticity, thermal conductivity and electrical conductivity (Sawchuk et al., 2021; Chao and Hsieh, 2019; Yao et al., 2018; Dasgupta and Hirschmann, 2006). Extensive experimental results have suggested that magnesite (MgCO_3) could be stable up to the core-mantle boundary pressure-temperature (P - T) conditions, hence it is expected as the main host phase of mantle carbon (Isshiki et al., 2004). Given the

abundance of iron in the mantle, the Mg/Fe substitution in magnesite is inevitable, thereby affecting the structural stability, density, elasticity, sound velocities and transport properties of carbonates in the mantle. According to established compositional model of the silicate Earth, the average molar ratio of Fe to Mg in the mantle ($\text{Fe}/(\text{Fe} + \text{Mg})$) is 0.12–0.15 (Lee et al., 2004; McDonough and Sun, 1995). Furthermore, the partitioning behaviors of Fe and Mg between carbonates and other major minerals provide compelling clues on the chemical composition of (Mg, Fe) CO_3 in the Earth's mantle. There is evidence that the magnesium-rich (Mg, Fe) CO_3 is likely to be more prevalent in the depths of the earth, since iron strongly partitions into ferropericlase rather than coexisting magnesite at relevant P - T conditions of the Earth's mantle (Palyanov et al., 2013). Based on the partial melting experiments of carbonated peridotite and eclogite (Dasgupta et al., 2004), approximately 20 mol% iron is dissolved in magnesite at relevant high P - T conditions to produce iron-bearing magnesite ($\text{Mg}_{0.8}\text{Fe}_{0.2}$) CO_3 , which provides valid evidence to estimate the realistic chemical composition of ferromagnesite in the deep Earth.

*Corresponding author: sqin@pku.edu.cn

© China University of Geosciences (Wuhan) and Springer-Verlag GmbH Germany, Part of Springer Nature 2024

Manuscript received April 23, 2021.

Manuscript accepted June 9, 2021.

Over the last few decades, the high P - T properties of (Mg, Fe)CO₃ of different composition have been studied by several experimental methods, including XRD, X-ray emission spectroscopy, visible and X-ray Raman spectroscopy, infrared spectroscopy, and Mössbauer spectroscopy (Chariton et al., 2020; Cerantola et al., 2017; Taran et al., 2017; Weis et al., 2017; Lobanov et al., 2016, 2015; Merlini et al., 2016, 2015; Müller et al., 2016; Cerantola et al., 2015; Liu et al., 2014; Spivak et al., 2014; Boulard et al., 2012, 2011; Farfan et al., 2012; Lin et al., 2012; Lavina et al., 2010a, b, 2009; Nagai et al., 2010; Mattila et al., 2007; Santillán, 2005; Zhang et al., 1998). Zhang et al. (1998) investigated the thermoelastic properties of FeCO₃ and (Fe_{0.6}Mg_{0.38}Mn_{0.02})CO₃ at pressures and temperatures up to 8.9 GPa and 1 073 K. A linear increase of the room-temperature bulk modulus with increasing iron content in (Mg, Fe)CO₃ was observed, yet it deviates from the empirical prediction that the product of K_0 and V_0 is constant. Later, more attention was drawn to the electronic high spin (HS) to low spin (LS) transition of iron bearing carbonates at high P - T conditions. Mattila et al. (2007) first described the spin transition with a reduction of total spin momentum in Fe²⁺ of natural siderite (Fe_{0.96}Mn_{0.04})CO₃ to occur at roughly 50 GPa by K β X-ray emission spectroscopy. The spin transition of Fe²⁺ in (Mg, Fe)CO₃ has been well constrained to occur at 40–55 GPa and 300 K associated with a 3%–10% reduction in the unit-cell volume of varied components using high-pressure X-ray, laser optical spectroscopic techniques and theoretic calculations (Chariton et al., 2020; Weis et al., 2017; Hsu and Huang, 2016; Müller et al., 2016; Cerantola et al., 2015; Liu et al., 2014; Spivak et al., 2014; Farfan et al., 2012; Lin et al., 2012; Lavina et al., 2010a, b, 2009; Nagai et al., 2010). However, there is still debate on the starting pressure and pressure ranges of the Fe²⁺ spin transition, whether the spin transition relates to composition and how the impurity elements in natural samples affect the transition. Besides, siderite and iron bearing magnesite have attracted wide interest in their phase transformations into novel phases Fe₄C₃O₁₂ and (Mg, Fe)₄C₄O₁₃ (Cerantola et al., 2017; Merlini et al., 2015; Boulard et al., 2012, 2011) with corner-sharing (CO₄)⁴⁻ tetrahedra and sp³-bonded carbon at pressures exceeding 40 GPa and high temperature (Lobanov and Goncharov, 2020). Structural differences between three-membered and four-membered rings of tetrahedral (CO₄)⁴⁻ units indicate that the stability field of (Mg, Fe)CO₃ is strongly associated with composition. In general, previous studies mainly focus on the iron-rich ferromagnesite with a more significant spin transition and structural change due to the presence of iron, especially the more accessible natural siderite containing impurities of Mn and Ca.

In this study, we have synthesized carbonate samples with 19 mol% iron, so as to simulate the mantle composition carbonates. The compressibility and vibrational properties of synthetic impurity free sample of (Mg_{0.81}Fe_{0.19})CO₃ have been investigated by single crystal XRD and Raman spectroscopy in a diamond-anvil cell (DAC). Knowledge of its high-pressure behavior in the deep Earth is a key to interpret the roles of ferromagnesite with 19 mol% iron as a potential carbon carrier in the evolution of the interior of the Earth as well as the mantle's role in the global carbon cycle.

1 EXPERIMENTAL METHODS

1.1 Sample Preparation

The ferromagnesite single crystals were prepared by high P - T annealing as reported by Liang et al. (2018a) and the details are presented in Supplementary Material A. The chemical composition of ferromagnesite was determined to be (Mg_{0.81}Fe_{0.19})CO₃ using a JEOL JXA-8100 electron microprobe at the Institute of Geology, Chinese Academy of Geological Sciences, as shown in Figure S1. The XRD analyses confirmed the R $\bar{3}c$ structure of (Mg_{0.81}Fe_{0.19})CO₃, with lattice parameters $a = 4.647 1 (2) \text{ \AA}$, $c = 15.101 (2) \text{ \AA}$, and $V = 282.45(3) \text{ \AA}^3$ at ambient conditions.

1.2 High-Pressure *in-situ* Synchrotron XRD

A symmetric diamond-anvil cell (DAC) was mounted with a pair of diamond anvils of 300 μm flat culets and a pre-indented Re gasket with a hole as sample chamber (180 μm in diameter and 30 μm in thickness). A piece of single crystal (Mg_{0.81}Fe_{0.19})CO₃ with both sides polished (a diameter of $\sim 35 \mu\text{m}$ and a thickness of $\sim 7 \mu\text{m}$) was loaded into the sample chamber along the (101) crystal plane facing the incident laser beam, together with several ruby spheres and a piece of gold close to the sample as the pressure calibrant. The pressure-transmitting medium, Ne, was loaded into the sample chamber in the high-pressure gas loading system of GSECARS/COMPRES. High-pressure XRD experiments were carried out at beamline 13-BM-C of the APS, ANL, USA. The incident X-ray beam had a wavelength of 0.433 5 \AA and a focal spot size of $15 \times 15 \mu\text{m}^2$. Diffraction images were acquired with a PILATUS3 1M (Dectris) detector. The tilting and rotation of the MarCCD detector relative to the incident X-ray beam were calibrated using lanthanum hexaboride (LaB₆) powder as the XRD standard. XRD images were processed and integrated using the Dioptas software to derive the lattice parameters of the sample and the Au pressure calibrant. Pressure was calculated using a third-order BM EoS of Au (Fei et al., 2007).

1.3 High-Pressure Raman Spectroscopy

High-pressure Raman spectra of (Mg_{0.81}Fe_{0.19})CO₃ were collected from 150–1 300 cm^{-1} with a Renishaw inVia Reflex system in a back-scattering geometry at Peking University. The Raman signal was excited using the 532 nm wavelength of a diode-pumped solid-state laser, delivering an emission power of $\sim 50 \text{ mW}$ focused onto an approximately 2.5 μm spot by a $20 \times$ long-distance objective. Spectral resolution was about 1 cm^{-1} with the holographic diffraction grating of 1 800 lines/mm. The spectra were calibrated using a silicon wafer. A piece of single crystal of (Mg_{0.81}Fe_{0.19})CO₃ with a diameter of $\sim 40 \mu\text{m}$ and a thickness of $\sim 12 \mu\text{m}$ was loaded inside a symmetric DAC together with a few ruby spheres. The assembly is the same as that of the *in-situ* synchrotron XRD described above. Neon was loaded into the sample chamber in the high-pressure gas loading system of GSECARS/COMPRES as the pressure-transmitting medium. All Raman data were collected on the same single crystal with invariant orientation up to the target pressure. Pressure was determined by multiple measurements of the wavelength of the ruby fluorescence before and after each experimental run (Shen et al., 2020).

2 RESULTS AND DISCUSSION

2.1 High-Pressure XRD and Compressibility of ($\text{Mg}_{0.81}\text{Fe}_{0.19}\text{CO}_3$)

The XRD patterns of ($\text{Mg}_{0.81}\text{Fe}_{0.19}\text{CO}_3$) were collected up to 53 GPa at the room temperature (Figure 1), no structural transition was identified as no peak-appearance/elimination was observed. The lattice parameters were calculated through the refinement of high-pressure XRD pattern (Figure 2a; Table 1). The unit cell volume underwent a distinct collapse of approximately 1.8% at ~44 GPa due to the spin transition of Fe^{2+} . It is almost equal to 20% of that of FeCO_3 (Lavina et al., 2010b) and thus the collapse volume per unit iron content could be a constant. The compressibility of ferromagnesite ($\text{Mg}_{0.81}\text{Fe}_{0.19}\text{CO}_3$) has been evaluated by fitting the bulk modulus at ambient pressure (K_0) and its pressure derivative (K'_0) of the BM-EoS to the pressure-volume data in the high spin state (Birch, 1978):

$$P = \frac{3K_0}{2} \left[\left(\frac{V_0}{V} \right)^{\frac{7}{3}} - \left(\frac{V_0}{V} \right)^{\frac{5}{3}} \right] \left[1 - \frac{3}{4} (4 - K'_0) \left[\left(\frac{V_0}{V} \right)^{\frac{2}{3}} - 1 \right] \right] \quad (1)$$

where K_0 , K'_0 , and V_0 are the isothermal bulk modulus, its pressure derivative, and the unit cell volume, respectively. The compressibility of high spin state was quantified, resulting in K_0

= 110.8(4) GPa for a second-order BM-EoS and $K_0 = 108(1)$ GPa with $K'_0 = 4.2(1)$ for a third-order BM-EoS, respectively. To further describe the compressive behavior, the relation between the volume Eulerian finite strain ($f_E = [(V_0/V)^{2/3} - 1]/2$) and the “normalized pressure” ($F_E = P/[3f_E(2f_E + 1)^{5/2}]$) was determined and shown in Figure 2b (Angel, 2000). The intercept $F_E(0)$ achieved by the weighted linear regression is an important criterion of quantified compressibility, and the value of $F_E(0) = 109(1)$ GPa is in good agreement with the K_0 derived from the Birch-Murnaghan equation. Likewise, the f_E - F_E plot exhibits a clear transition in the compressional behavior at 44–50 GPa, corresponding to the occurrence of spin transition. The normalized lattice parameters (a/a_0 and c/c_0) are adopted to reveal the anisotropy of the axial compressibility, as presented in Figure S2. The axial compressibility along a and c is fitted by the third-order Birch-Murnaghan equation (Birch, 1978), resulting in $K_0 = 154.0(7)$ GPa with $K'_0 = 7.1(1)$ for the a axis and $K_0 = 66.0(2)$ GPa with $K'_0 = 2.84(2)$ for the c axis.

The P - V relationship for a range of composition in MgCO_3 - FeCO_3 system from the previous results was plotted into Figure 2a to compare the compressibility of the high spin state (Chariton et al., 2020; Liu et al., 2014; Farfan et al., 2012; Lin et al., 2012; Lavina et al., 2010a, b, 2009; Nagai et al., 2010; Fiquet et al., 2002; Zhang et al., 1998), and the relevant

Table 1 Equation of state parameters of $\text{Mg}_{1-x}\text{Fe}_x\text{CO}_3$ at high pressures from this and previous studies

Composition	V_0 (\AA^3)	K_0 (GPa)	K'_0	$\Delta V/V_0$ (%) ^a	Transition pressure (GPa)	Technique ^b	Reference
($\text{Mg}_{0.81}\text{Fe}_{0.19}\text{CO}_3$) CO_3	282.43(5)	108(1)	4.2(1)	1.8	44–46	SCXRD; DAC(Ne)	This study
MgCO_3	279.3(2)	103(1)	4	—	—	XRD; LVA	Zhang et al. (1997)
MgCO_3 (natural)	279.2(2)	108(3)	5.0(2)	—	—	Powder XRD; DAC	Fiquet et al. (2002)
($\text{Mg}_{0.994}\text{Ca}_{0.006}\text{CO}_3$) CO_3	---	103(2)	5	—	—	Powder XRD; DAC(Ne)	Isshiki et al. (2004)
($\text{Mg}_{0.99}\text{Fe}_{0.01}\text{CO}_3$) CO_3	279.0(5)	113(1)	4	—	—	SCXRD; DAC(Ne/He)	Merlini et al. (2016)
($\text{Mg}_{0.975}\text{Fe}_{0.015}\text{Mn}_{0.006}\text{Ca}_{0.004}\text{CO}_3$) CO_3	279.55(2)	97.1(5)	5.44(7)	—	—	Powder XRD; LVA	Litasov et al. (2008)
($\text{Mg}_{0.89}\text{Fe}_{0.11}\text{CO}_3$) CO_3	280.9(2)	115.9(9)	4	—	—	SCXRD; DAC(Ne/He)	Merlini et al. (2016)
($\text{Mg}_{0.87}\text{Fe}_{0.12}\text{Ca}_{0.01}\text{CO}_3$) CO_3	281.0(5)	102.8(3)	5.44	—	49–52	SCXRD; DAC(Ne)	Lavina et al. (2010a)
($\text{Mg}_{0.74}\text{Fe}_{0.26}\text{CO}_3$) CO_3	282.69(8)	112(1)	4.3(1)	3	44	SCXRD; DAC(Ne)	Chariton et al. (2020)
($\text{Fe}_{0.60}\text{Mg}_{0.38}\text{Mn}_{0.02}\text{CO}_3$) CO_3	288.3(1)	112(1)	4	—	—	XRD; LVA	Zhang et al. (1998)
($\text{Fe}_{0.65}\text{Mg}_{0.33}\text{Mn}_{0.02}\text{CO}_3$) CO_3	289.1(1)	108(2)	4.8(2)	8	45	SCXRD; DAC(Ne)	Lin et al. (2012)
($\text{Fe}_{0.65}\text{Mg}_{0.33}\text{Mn}_{0.02}\text{CO}_3$) CO_3	289.2(1)	109(1)	4.9(2)	6.5	43.4–47.5	SCXRD; DAC(Ne)	Liu et al. (2014)
($\text{Fe}_{0.70}\text{Mg}_{0.26}\text{Mn}_{0.025}\text{Ca}_{0.015}\text{CO}_3$) CO_3	288.0(4)	123(1)	4	—	—	SCXRD; DAC(Ne/He)	Merlini et al. (2016)
($\text{Fe}_{0.72}\text{Mn}_{0.24}\text{Mg}_{0.03}\text{Ca}_{0.01}\text{CO}_3$) CO_3	—	—	—	9	42–44	SCXRD; DAC	Lavina et al. (2009)
($\text{Fe}_{0.73}\text{Mg}_{0.22}\text{Mn}_{0.05}\text{CO}_3$) CO_3	293.5(1)	120(3)	4.3	6.5	47–50	Powder XRD; DAC(Ar)	Nagai et al. (2010)
($\text{Fe}_{0.74}\text{Mg}_{0.21}\text{Mn}_{0.04}\text{Ca}_{0.01}\text{CO}_3$) CO_3	291.0(8)	125(2)	4	—	—	SCXRD; DAC(Ne/He)	Merlini et al. (2016)
($\text{Fe}_{0.76}\text{Mn}_{0.15}\text{Mg}_{0.09}\text{Ca}_{0.01}\text{CO}_3$) CO_3	—	—	—	8	46	Powder XRD; DAC(None)	Farfan et al. (2012)
($\text{Fe}_{0.95}\text{Mn}_{0.045}\text{Mg}_{0.005}\text{CO}_3$) CO_3	293.4(2)	117.7(9)	4	—	—	SCXRD; DAC(Ne/He)	Merlini et al. (2016)
($\text{Fe}_{0.96}\text{Mg}_{0.04}\text{CO}_3$) CO_3	294.4(3)	110(2)	4.6(2)	10	44–45	SCXRD; DAC(Ne)	Lavina et al. (2010b)
($\text{Fe}_{0.998}\text{Mn}_{0.002}\text{CO}_3$) CO_3	292.83(4)	117(1)	4	—	—	XRD; LVA	Zhang et al. (1998)
FeCO_3	292.15(5)	97.5(11)	4	—	—	SCXRD; DAC(Ne)	Liang et al. (2018b)
FeCO_3	292.66(2)	125(3)	3.8(2)	10	44	SCXRD; DAC(Ne)	Chariton et al. (2020)
FeCO_3	291.81	108	4.5(1)	—	—	Theory	Badaut et al. (2010)

^a $\Delta V/V$ is the percentage of the volume decrease across the spin transition. ^b SCXRD. Single crystal X-ray diffraction; XRD. X-ray diffraction; DAC. diamond-anvil cell (we also mark the pressure medium used in the experiment in brackets, such as Ne for Neon, Ar for Argon and None for no pressure medium); LVA. large volume apparatus.

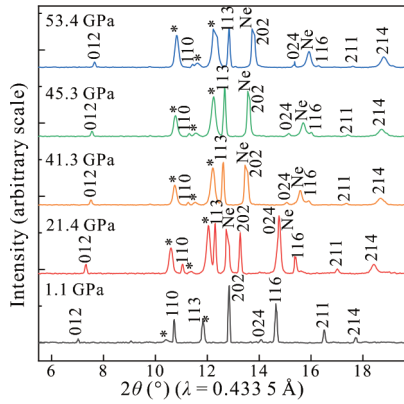


Figure 1. Representative XRD spectra of ferromagnesite ($\text{Mg}_{0.81}\text{Fe}_{0.19}\text{CO}_3$) at high pressure. The asterisks (*) symbolize the signal coming from the Re gasket due to the relatively large incident spot. Incident X-ray wavelength $\lambda = 0.4335 \text{ \AA}$.

K_0 was summarized in Table 1. The 1 bar and 300 K bulk moduli with K' fixed to 4 for high spin Fe^{2+} derived from previous XRD experiments (Chariton et al., 2020; Liang et al., 2018b; Merlini et al., 2016; Zhang et al., 1998, 1997) was plotted in Figure S3. There is still controversy on the relationship of iron content and K_0 . Zhang et al. (1998) reported a trend that K_0 increases as the increase of iron content, which suggests that FeCO_3 with the longer bond length (Fe-O) is less compressible than MgCO_3 . However, it deviates from the empirical inverse correlation prediction that the product of K_0 and V_0 is regarded to be constant (Hazen and Prewitt, 1977). Subsequently, Merlini et al. (2016) found an irregular compressional behavior in natural samples of $\text{MgCO}_3\text{-FeCO}_3$ system; that is, the K_0 increases with the increase of iron content from 0.01% to 74% but the value for endmember FeCO_3 is lower than samples with 70% and 74% iron content. Most recently, the K_0 of impurity-free FeCO_3 was reported to be 97.5 GPa ($K' = 4$), the lowest value for magnesiosiderite reported so far, which casts doubt upon the anomalous compression mechanism (Liang et al.,

2018b). Our experimental results on the compressibility of synthetic ($\text{Mg}_{0.81}\text{Fe}_{0.19}\text{CO}_3$), without the impurities common to natural ferromagnesite, provide a reliable reference for $\text{MgCO}_3\text{-FeCO}_3$ system. The compression mechanism, as well as the nonlinear relation of compressibility and iron content, is thus proposed to verify and optimize using synthetic continuous solid solutions for further systematic research.

2.2 High-Pressure Raman Spectroscopy and Vibrational Properties of ($\text{Mg}_{0.81}\text{Fe}_{0.19}\text{CO}_3$)

The Raman vibrations that offer complementary information about the crystal structure and calcite-type carbonates have been extensively studied. According to factor group analyses, calcite-type carbonates with rhombohedral primitive cell containing 10 atoms per lattice point have 27 vibrational modes. Among them, the translational (T) and librational (L) modes in low-frequency region represent external modes, resulting from the interactions between M^{2+} and CO_3^{2-} ions. The high-frequency vibrational modes, ν_4 (in-plane bend), ν_1 (symmetric stretch), ν_3 (anti-symmetric stretch) and $2\nu_2$ (out-of-plane bend, overtone mode of the silent, IR-active ν_2 mode) represent internal modes of the CO_3^{2-} group (Farsang et al., 2018; Rividi et al., 2010; Rutt and Nicola, 1974). High-pressure Raman spectra of ($\text{Mg}_{0.81}\text{Fe}_{0.19}\text{CO}_3$) were measured in 1–2 GPa intervals up to 52 GPa at room temperature (Figure 3a), in which ν_3 and $2\nu_2$ modes were not observed owing to limitations in the diamond windows. The measured Raman modes (T , L , ν_4 , and ν_1) recorded a linear peak shift as a function of pressure from zero pressure to 23 GPa (Figure 3b; Table 2). The trend of intensity ratio and full width at half maximum (FWHM) of each mode were analyzed to provide the relevant evolutions in local structures (Figure S4).

A slight decrease in ν_1 mode and the increase in other modes, without any significant peak splitting, were observed across the spin transition at 47 GPa. The decrease in ν_1 mode could be caused by the elongation effect of C-O bond which is greater than that of lattice contraction (Lavina et al., 2010b),

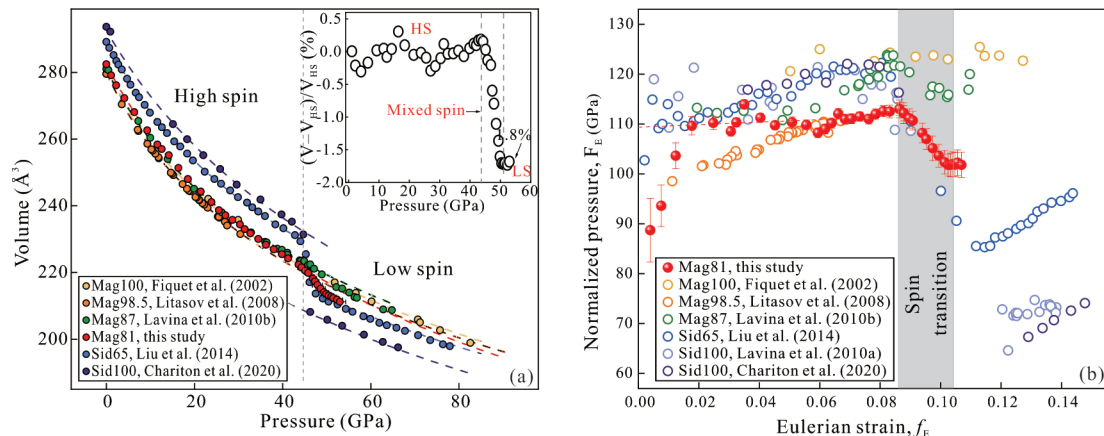


Figure 2. (a) Comparison of the pressure-volume relations in the system of $\text{MgCO}_3\text{-FeCO}_3$ solid solution (Chariton et al., 2020; Liu et al., 2014; Lavina et al., 2010b; Litasov et al., 2008; Fiquet et al., 2002). Dashed lines represent BM-EoS fits to the high and low spin state of different compositions at 300 K. The inserted figure at the top right shows the spin crossover diagram of our ($\text{Mg}_{0.81}\text{Fe}_{0.19}\text{CO}_3$) sample and the volume differences between the experimental P - V data and the modeled HS P - V curve. The volume collapse across the spin transition is 1.8% in this study. (b) Eulerian strain-normalized pressure ($F'_E - F_E$) plot of unit cell volume of $\text{Mg}_{1-x}\text{Fe}_x\text{CO}_3$ with different iron contents. Linear fits of the data yield the intercept values of $F'_{E_V}(0) = 109(1) \text{ GPa}$ ($< 40 \text{ GPa}$) in this study.

Table 2 Modeled vibrational parameters of ferromagnesite ($\text{Mg}_{0.81}\text{Fe}_{0.19}\text{CO}_3$) and other iron-rich carbonates at high pressures from this and previous studies

Raman	Mag81 ^a		Mag100 ^b		Mag96 ^c		Sid65 ^d		Sid100 ^e		Sid100 ^f	
	dv/dP	γ_i	dv/dP	γ_i	dv/dP	γ_i	dv/dP	γ_i	dv/dP	γ_i	dv/dP	γ_i
T	2.89(6)	1.52(3)	3.08(5)	1.49(2)	3.52(3)	1.76	2.51(10)	1.36(5)	2.99(2)	1.61(1)	2.51	1.18
L	4.03(8)	1.38(2)	4.49(5)	1.40(2)	4.89(3)	1.59	3.64(18)	1.25(6)	4.01(2)	1.39(1)	3.82	1.16
ν_4	1.69(2)	0.25(1)	1.83(2)	0.26(1)	1.52(4)	0.22	1.49(6)	0.22(1)	2.00(2)	0.27(1)	1.37	0.21
ν_1	2.66(2)	0.27(1)	2.87(2)	0.27(1)	2.87(4)	0.28	2.17(7)	0.21(1)	2.46(1)	0.22(1)	2.17	0.22

^aMag81. ($\text{Mg}_{0.81}\text{Fe}_{0.19}\text{CO}_3$, this study. The measured initial frequencies of Raman modes for ($\text{Mg}_{0.81}\text{Fe}_{0.19}\text{CO}_3$) at 0 GPa and the bulk moduli K_0 set as 110.8 GPa are chosen to derive the mode Grüneisen parameters γ_i , dv/dP in the unit of $\text{cm}^{-1}/\text{GPa}$; γ_i , mode Grüneisen parameters; ^bMag100. $\text{Mg}_{0.999\pm 0.001}\text{CO}_3$, Liang et al. (2018a); ^cMag96. $\text{Mg}_{0.96}\text{Ca}_{0.01}\text{Fe}_{0.03}\text{CO}_3$, Farsang et al. (2018); ^dSid65. ($\text{Fe}_{0.65}\text{Mg}_{0.33}\text{Mn}_{0.02}\text{CO}_3$, Lin et al. (2012); ^eSid100. $\text{Fe}_{0.999\pm 0.001}\text{CO}_3$, Liang et al. (2018b); ^fSid100. Synthesized FeCO_3 , Cerantola et al. (2015).

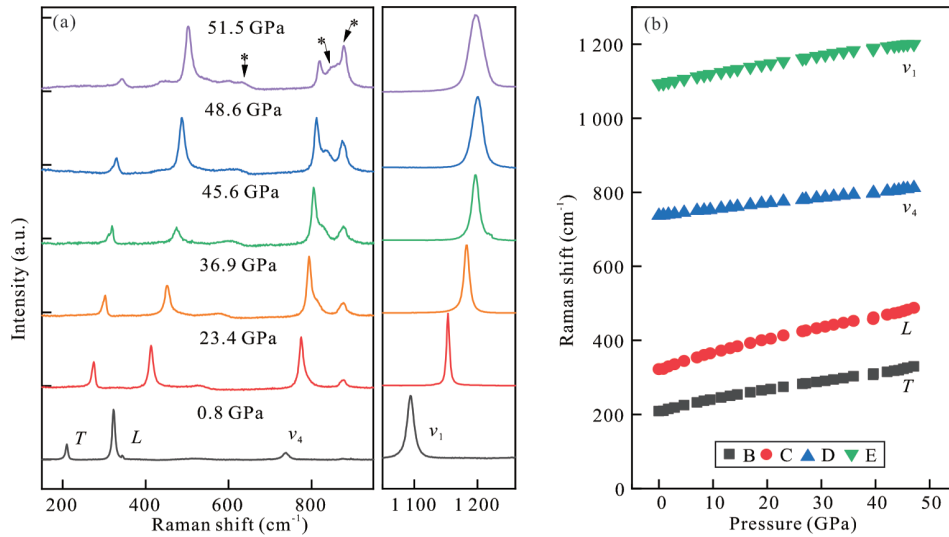


Figure 3. (a) Representative Raman spectra of ferromagnesite ($\text{Mg}_{0.81}\text{Fe}_{0.19}\text{CO}_3$) at high pressure. The Raman mode was labeled according to Farsang et al. (2018). T , Translational mode; L , librational mode; ν_4 , in-plane bend internal mode; ν_1 , symmetric stretch internal mode. The asterisks (*) symbolize the Raman peaks likely related to Mg-Fe substitution. (b) Raman shifts of each mode as a function of pressure can be modeled by a linear fit from zero pressure to 23 GPa.

whereas the increase of T , L and ν_4 modes is mainly contributed from the fact that the low spin state exhibits a stiffer unit-cell lattice and smaller bond distances due to its relatively smaller radius of Fe^{2+} (Cerantola et al., 2015; Lin et al., 2012; Lavina et al., 2010a, b, 2009; Nagai et al., 2010). Moreover, the FWHM values of the ν_1 mode increase sharply across spin transition (in Figure S4), which is consistent with the results reported by Muller et al. (2016). It could be interpreted as local structural disorder, inhomogeneities, defects or a modified vibrational density of states during spin transition. In addition to Raman peaks characteristic for calcite-type carbonates, two new Raman peaks (784 and 875 cm^{-1}) began to appear at 23 GPa and became more pronounced with increased pressure, thereby causing uncertainties in the determination of ν_4 peak position. These unassigned peaks have been attributed by Langille and Oshea (1977) to an infrared mode becoming Raman active due to a local loss of inversion symmetry as a result of Fe ordering (Langille and Oshea, 1977).

Combined the $K_0 = 110.8$ GPa from EoS with the high-pressure Raman results of dv/dP , the mode Grüneisen parameters γ_i for each vibration mode were derived according to the equation as follows

$$\gamma_i = -\frac{d \ln \nu_i}{d \ln V} = \frac{K_T}{\nu_{i,0}} \left(\frac{d \nu_i}{d P} \right) \quad (2)$$

where γ_i is the mode Grüneisen parameter, K_T is isothermal bulk model, and $\nu_{i,0}$ is the frequency of each mode at the ambient conditions.

The derived mode Grüneisen parameters were listed in Table 2, together with previous results for comparison. The mode Grüneisen parameters for the two lattice modes (T and L) are 1.52 and 1.38, and for the two internal modes (ν_4 and ν_1) are 0.25 and 0.27. The values of parameters for two external modes (T and L) are approximately five times greater than those of the higher frequency internal modes (ν_4 and ν_1), revealing that the compression of calcite-type carbonates is mainly dominated by the coordinated octahedra linked the $[\text{CO}_3]^{2-}$ groups to the cations (Williams et al., 1992). Furthermore, there is a decreasing trend with the increase of iron content for the values of the mode Grüneisen parameters for two external modes (T and L) which related to metal cations while the parameters barely change with the variation of iron content for two internal modes (ν_4 and ν_1) (Figure 4a, Farsang et al., 2018; Liang et al., 2018a, b; Cerantola et al., 2015; Lin et al., 2012).

However, there are still a few data points deviating from the overall trend, which may arise from differences in the quality of Raman data acquisition and processing as well as the interferences of impurities (Ca^{2+}) in natural samples.

For a more quantitative comparison on the effect of iron doping on the vibrational properties of solid solutions before spin transition, we build the model of Raman shift of ν_1 mode as the Fe content increasing up to 40 GPa combining the Raman data of $\text{Mg}_{1-x}\text{Fe}_x\text{CO}_3$ with different iron contents in the literature (Liang et al., 2018a, b; Lin et al., 2012) (Figure 4b). The ν_1 mode is the most intense mode in the spectrum and its change against pressure is relatively obvious due to it is directly related to the C-O bond, making it the best candidate to calibrate the peak position. The Raman shift decreases when the Fe^{2+} substitutes Mg^{2+} in the structure, since the ion radius of Fe^{2+} (high spin) is a little bit bigger and heavier than Mg^{2+} , thereby increasing the interatomic distances between the Mg^{2+} , Fe^{2+} cation and the $(\text{CO}_3)^{2-}$ anion in the unit cell of magnesite. The peak position of ν_1 mode is relatively linear with the change of composition under ambient pressure, however, at higher pressure, the addition of iron can lead to a relatively large reduction of peak position. The linear relationship of ν_1 mode as a function of pressure between siderite FeCO_3 ($\nu_1(P) = 2.46P + 1084.49$), ferromagnesite $(\text{Mg}_{0.81}\text{Fe}_{0.19})\text{CO}_3$ ($\nu_1(P) = 2.66P + 1093.32$) and magnesite MgCO_3 ($\nu_1(P) = 2.87P + 1094.04$) are presented in Figure S5. The value of slope $d\nu_1/dP$ decreases as the iron content increase suggests a greater difference in ν_1 between MgCO_3 and FeCO_3 at higher pressure. The correlation between Raman spectra and the chemical composition of magnesite and siderite has potential applications in on-line measurement of high-pressure experiments and *in-situ* mineralogical determination in future planetary explorations.

2.3 Characterizations of the Fe^{2+} Spin Transition in Ferromagnesite at High Pressure

The spin transition of Fe^{2+} induced by the relevant high-pressure conditions has a major impact on the physical and

chemical properties of host minerals in the lower mantle, such as density, velocity, iron partitioning (Farfan et al., 2012; Lin et al., 2012; Lavina et al., 2010a, b, 2009; Nagai et al., 2010). It is thus quite important to establish the phase diagram for the spin transition as a function of the iron contents to display the heterogeneity of the mantle. Since Lavina et al. (2009) first observed the spin transition in the ferromagnesite, plenty of studies focused on the components with different iron contents, thereby inspiring the interest to emphasize the spin crossover as the characteristics of this potential deep carbon host (Figure S6). The spin crossover, which is common in iron-bearing minerals such as ferropicriase at high pressures, has been under discussion with regard to whether Fe^{2+} - Fe^{2+} exchange interactions occur in the ferromagnesite structure or not. The density functional theory calculations have predicted the consistent spin transition pressure for varied components of ferromagnesite (Hsu and Huang, 2016), which is attributed to the weak Fe^{2+} - Fe^{2+} exchange interactions in ferromagnesite because the corners-sharing $[\text{FeO}_6]$ octahedron is separated by $[\text{CO}_3]^{2-}$ leading to a relatively longer distance between neighboring Fe^{2+} ions in carbonates than the ferropicriase with the edges-sharing octahedral (Liu et al., 2020). Nevertheless, Spivak et al. (2014) performed Raman spectroscopy on synthetic ferromagnesite system and found that the front pressure of spin transition can shift to slightly higher pressures with the addition of Mg. In contrast to this, Weis et al. (2017) observed a comparable transition front and width of synthetic siderite and ferromagnesite $(\text{Mg}_{0.74}\text{Fe}_{0.26})\text{CO}_3$, illustrating that there is a negligible compositional effect on the spin transition pressure, which supports the results from theoretical calculations (Hsu and Huang, 2016). Likewise, our results of $(\text{Mg}_{0.81}\text{Fe}_{0.19})\text{CO}_3$ from XRD experiment revealing almost identical transition pressure (44–46 GPa) to the previous reports of iron-rich components also support that there is no spin transition pressure-composition correlation in the ferromagnesite. In contrast, the transition shifted to a higher pressure at 47 GPa based on the observation of Raman spectra. To eliminate the error caused by the selec-

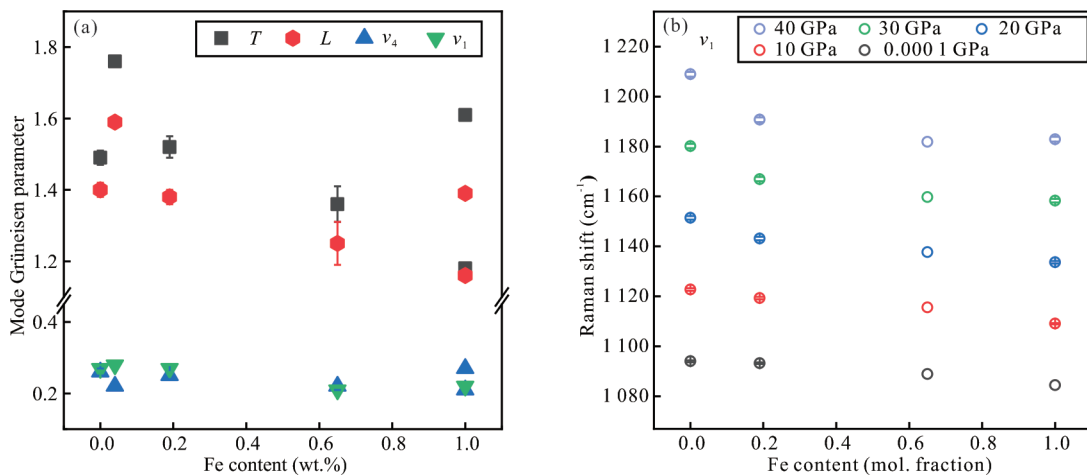


Figure 4. (a) The mode Grüneisen parameters of each vibration (T , L , ν_4 and ν_1) of MgCO_3 , $\text{Mg}_{0.96}\text{Ca}_{0.01}\text{Fe}_{0.03}\text{CO}_3$, magnesian siderite $(\text{Mg}_{0.35}\text{Fe}_{0.65})\text{CO}_3$, FeCO_3 and our results of ferromagnesite $(\text{Mg}_{0.81}\text{Fe}_{0.19})\text{CO}_3$ (Farsang et al., 2018; Liang et al., 2018a, b; Cerantola et al., 2015; Lin et al., 2012). (b) The Raman mode ν_1 of FeCO_3 , MgCO_3 , magnesian siderite $(\text{Mg}_{0.35}\text{Fe}_{0.65})\text{CO}_3$ (Liang et al., 2018a, b; Lin et al., 2012) as well as our results of ferromagnesite $(\text{Mg}_{0.81}\text{Fe}_{0.19})\text{CO}_3$ at pressures up to 40 GPa by a step of 10 GPa were plotted for comparison.

tion of pressure scales, we also employed models from Ye et al. (2018, 2017) for inter-calibrated Au-ruby P-scales. According to the inter-calibration, the difference between Au and ruby P-scale at high pressure around 50 GPa is within 0.3 GPa. Besides, the inconsistency of XRD and Raman results could be caused by the postponed observation of the onset of spin transition in Raman spectra, since it is not obvious with only a slight slope variation instead of the splitting ν_1 mode with low iron content. Consequently, the criterion achieved from the collapse of cell volume is believed to be more sensitive than that of Raman shift for the Mg-rich part of system.

2.4 High-Temperature and High-Pressure Behavior of ($\text{Mg}_{0.81}\text{Fe}_{0.19}\text{CO}_3$) in the Earth's Interior

We have calculated the high-temperature and high-pressure behavior of ($\text{Mg}_{0.81}\text{Fe}_{0.19}\text{CO}_3$) to model its influence on the mantle. The density and bulk sound velocity as a function of pressure of ($\text{Mg}_{0.81}\text{Fe}_{0.19}\text{CO}_3$) at 300 K was plotted in Figures 5a and 5b, along with ($\text{Mg, Fe}\text{CO}_3$) with varied iron content for comparison (Chariton et al., 2020; Liu et al., 2014; Lavina et al., 2010b; Fiquet et al., 2002). The density (ρ) can be determined by molar mass and the unit-cell volume, whereas the bulk sound velocity (V_ϕ) can be calculated using the Eq. (3)

$$V_\phi = \sqrt{K_s/\rho} \quad (3)$$

where K_s is the adiabatic bulk modulus. For simplification, we use the value of isothermal bulk modulus K_T at 300 K for an approximate estimation of K_s of varied components.

The isothermal bulk modulus K_T can be calculated using the Eq. (4)

$$K_T = (1 + 2f)^{5/2} [K_0 + (3K_0K_0' - 5K_0)f + \frac{27}{2} (K_0K_0' - 4K_0)f^2] \quad (4)$$

where K_0 , K_0' and f are the isothermal bulk modulus, its pressure derivative, and the volume Eulerian finite strain, respectively, at ambient P and T .

Subducting slabs are proposed to be major carriers of carbonates to the deep Earth. With the Fe^{2+} substitution for Mg^{2+} in $\text{MgCO}_3\text{-FeCO}_3$ system, the ρ increases by approximately 31.2% from magnesite to siderite, whereas the V_ϕ of magnesite is higher than that of siderite by $\sim 2.9\%$ at ambient pressure and $\sim 8.1\%$ at pressure of the top of lower mantle, respectively. ($\text{Mg}_{0.81}\text{Fe}_{0.19}\text{CO}_3$) is relatively $\sim 6.1\%$ heavier than magnesite, making it much easier to be carried into the Earth's interior. To understand the geophysical and geodynamic significance of our results in a subducted slabs, we have evaluated ρ and V_ϕ profiles of ferromagnesite ($\text{Mg}_{0.81}\text{Fe}_{0.19}\text{CO}_3$) as a function of pressure along a 300, 1 200 and 1 500 K isotherm. To estimate

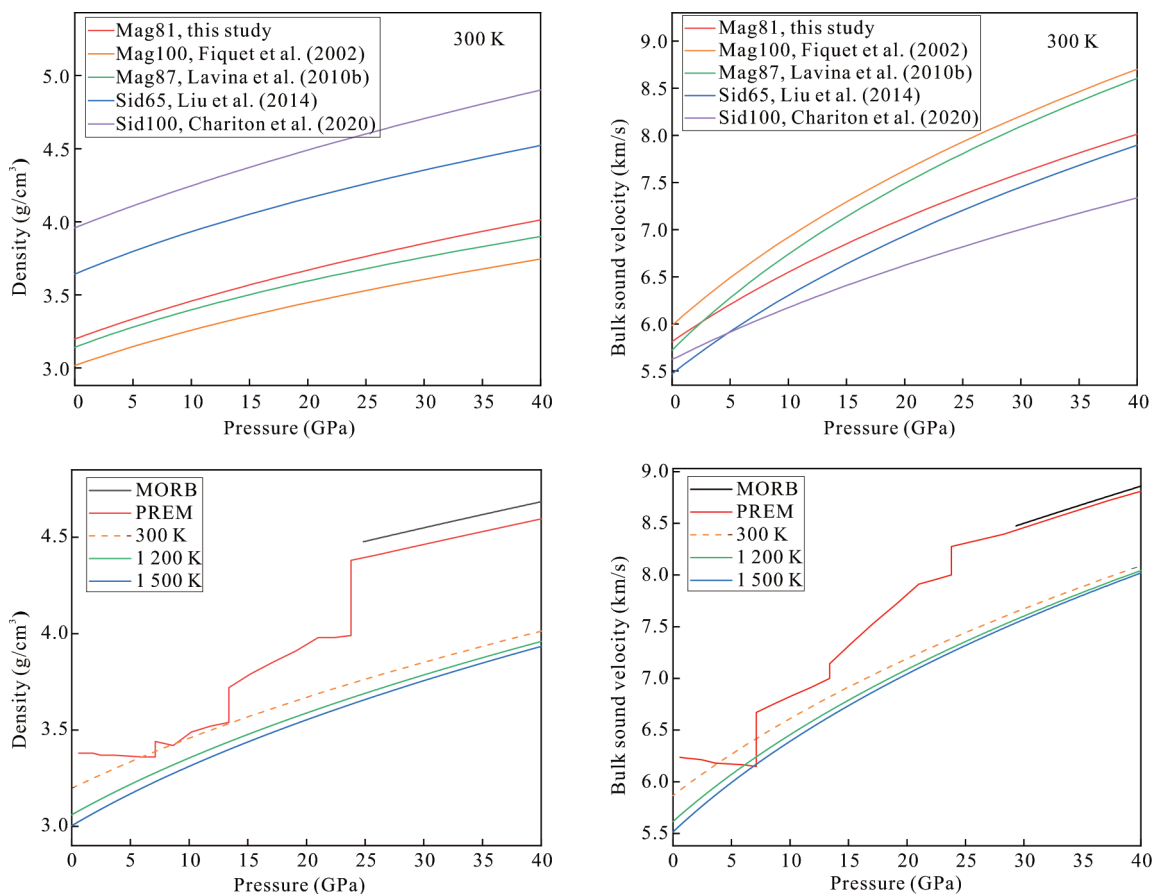


Figure 5. The 300 K (a) density and (b) bulk sound velocity as function of pressure of $\text{Mg}_{1-x}\text{Fe}_x\text{CO}_3$ with varied iron content from this and previous studies (Chariton et al., 2020; Liu et al., 2014; Lavina et al., 2010b; Fiquet et al., 2002). Modeled (c) density and (d) bulk sound velocity profiles of ferromagnesite ($\text{Mg}_{0.81}\text{Fe}_{0.19}\text{CO}_3$) from zero pressure to 40 GPa, at 300, 1 200 and 1 500 K, respectively compared to PREM model (red line) (Dziewonski and Anderson, 1981) and MORB at 2 000 K (black line) (Ricolleau et al., 2010).

P - V data at given temperatures, the third-order isothermal HT-BM equation was employed to derive the thermal parameters by the following expression for

$$P(V, T) = \frac{3K_{T0}}{2} \left[\left(\frac{V_{T,0}}{V} \right)^{\frac{7}{3}} - \left(\frac{V_{T,0}}{V} \right)^{\frac{5}{3}} \right] \left[1 - \frac{3}{4} (4 - K'_{T0}) \left[\left(\frac{V_{T,0}}{V} \right)^{\frac{2}{3}} - 1 \right] \right] \quad (5)$$

where K_{T0} is the isothermal bulk modulus at ambient pressure and a given temperature, $V_{T,0}$ is the ambient pressure volume, V is the high pressure and temperature volume, and K'_{T0} is the pressure derivative of K_{T0} at ambient pressure, neglecting higher-order pressure derivatives of the bulk modulus and assuming that K'_{T0} is a constant in the temperature range of our study. The temperature effect on K_T can be expressed as a linear function of temperature, with the temperature derivative at ambient pressure ($\partial K_T / \partial T$)_p and K_{T0} as follow

$$K_T = K_{T0} + (\partial K_T / \partial T)_p (T - T_0) \quad (6)$$

where T_0 is the reference temperature of 300 K. ($\partial K_T / \partial T$)_p is assumed to be a constant within the temperature range of our study. Using the value ($\partial K_T / \partial T$)_p = -0.021 GPa/K for an approximate estimation (Zhang et al., 1997). The temperature dependence of the volume at ambient pressure, $V_{T,0}$ can be expressed as a function of the thermal expansion at zero pressure

$$V_{T,0} = V_0 \exp \left(\int_{T_0}^T \alpha_T dT \right) \quad (7)$$

where α_T is the thermal expansion coefficient at high temperature and ambient pressure. In our model here, α_T is assumed to be a linear function of temperature

$$\alpha_T = \alpha_0 + \alpha_1 T \quad (8)$$

where α_0 and α_1 are constants, using values of $\alpha_0 = 3.15 \times 10^{-5} \text{ K}^{-1}$ and $\alpha_1 = 2.3 \times 10^{-8} \text{ K}^{-2}$ of magnesite for an approximate estimation (Zhang et al., 1997). With the derived K_T and α at a given temperature, the bulk sound velocity (V_ϕ) can be calculated using Eq. (3) and the following Eq. (9)

$$K_s = K_T (1 + \alpha \gamma T) \quad (9)$$

where K_s and K_T are the adiabatic and isothermal bulk modulus respectively, α is the thermal expansion coefficient at high temperature and ambient pressure, and γ is the thermodynamic Grüneisen parameter.

We used the following equation to calculate the γ value at ambient and high P - T conditions.

$$\gamma = \frac{\alpha K_s}{\rho C_p} \quad (10)$$

$$\gamma = \frac{\alpha K_T}{\rho C_v} \quad (11)$$

where α is the thermal expansion coefficient, K_s is the adiabatic bulk modulus, K_T is the isothermal bulk modulus, C_p is the heat capacity at constant pressure, C_v is the heat capacity at constant volume and ρ is the density. Using Eq. (10) and values of $\alpha = 3.84 \times 10^{-5} \text{ K}^{-1}$ (Zhang et al., 1997), $\rho = 3.197 \text{ g/cm}^3$ (this

study), $K_s = 115.7 \text{ GPa}$ (Sanchez-Valle et al., 2011), and $C_p = 82.44 \text{ J/(mol}\cdot\text{K)}$ (Robie et al., 1984) at 300 K, the calculated thermodynamic Grüneisen parameter of the high spin state is ~ 1.69 . Because the γ value of the ferromagnesite at high P - T remains unknown, we used Eq. (11) to estimate the γ value at high P - T conditions of 1 200 and 1 500 K. At high temperature, the molar heat capacity C_v approaches a constant of $3nR$, where n is number of atoms per formula and R is the gas constant. Here, we use the value of $C_v = 3nR = 124.671 \text{ J/(mol}\cdot\text{K)}$ for an approximate estimation at 1 200 and 1 500 K. The isothermal bulk modulus K_T and high P - T density is calculated accordingly.

The calculated ρ and V_ϕ of $(\text{Mg}_{0.81}\text{Fe}_{0.19})\text{CO}_3$ (0–40 GPa) are plotted in Figures 5c and 5d. The ρ profiles of $(\text{Mg}_{0.81}\text{Fe}_{0.19})\text{CO}_3$ are much lower than those of preliminary reference Earth model (PREM) and mid-ocean ridge basalt (MORB) (Ricolleau et al., 2010; Dziewonski and Anderson, 1981), indicating that the presence of carbonates could contribute to a positive buoyancy force in subducted slabs at the uppermost lower mantle conditions (Figure 5c). It is generally believed that ferromagnesite is more likely to be brought into the deep part of the earth with colder subduction (600 K cooler than normal mantle geotherm) (Syracuse et al., 2010). At 40 GPa, the density of $(\text{Mg}_{0.81}\text{Fe}_{0.19})\text{CO}_3$ in the colder subducted plate (~ 1 200 K) is about 18.3% less than that of the surrounding mantle rocks of MORB, revealing that the existence of Mg-rich ferromagnesite makes the subducted plate have greater buoyancy. For an overvalued carbon content of 0.5 wt.% (~ 3.8 wt.% for $(\text{Mg}_{0.81}\text{Fe}_{0.19})\text{CO}_3$) in altered oceanic crust in the colder subducted plate, the effect of $(\text{Mg}_{0.81}\text{Fe}_{0.19})\text{CO}_3$ on the density of the colder subducted plate is about 0.6%. Such a decrease has little effect on the buoyancy of the subducted plate, suggesting that the buoyancy of ferromagnesite that impedes the downward motion of the slab is not expected to significantly affect the dynamics of subducting slabs. For the wave velocity data, at 40 GPa, the bulk sound velocity of $(\text{Mg}_{0.81}\text{Fe}_{0.19})\text{CO}_3$ in the colder subducted plate (~ 1 200 K) is about 8.9% lower than that in the surrounding mantle rock, and about 9.3% in the hot subducted plate (300 K cooler than normal mantle geotherm, ~ 1 500 K). Such a reduction in the bulk sound velocity would result in a 0.3% reduction in seismic wave velocity. However, such a small anomaly in wave velocity is difficult to be observed in the seismic waves of the upper and lower mantle.

3 CONCLUSIONS

The high-pressure behavior of $(\text{Mg}_{0.81}\text{Fe}_{0.19})\text{CO}_3$ up to 53 GPa was studied by synchrotron X-ray diffraction and laser Raman spectroscopy and was further evaluated with thermodynamic modelling to reconstruct a much more vivid model of the deep carbon cycle. We detected the spin transition of $(\text{Mg}_{0.81}\text{Fe}_{0.19})\text{CO}_3$ by single-crystal X-ray diffraction with a concomitant volume decrease of 1.8% at around 44–46 GPa under quasi-hydrostatic conditions and observed significant changes of spin transition in vibrational Raman bands to a higher pressure above 47 GPa. Combined XRD and Raman results of this and previous studies, we concluded that there is no pressure-composition correlation on the spin transition pressure of $\text{Mg}_{1-x}\text{Fe}_x\text{CO}_3$ due to the weak Fe^{2+} - Fe^{2+} exchange interactions. Future researches with respect to the influence of iron composi-

tion of ferromagnesite system (Mg, FeCO_3) at relevant P - T conditions of the Earth's mantle will be carried out to provide an ideal model for the systematic carbonates investigation of crystal structure, elasticity and conductivity.

ACKNOWLEDGMENTS

We acknowledge the support from the National Natural Science Foundation of China (NSFC) (Nos. 41772034, 42072047, NSFC-41972056, NSFC-41622202 to G. B. Zhang, and the National Science Foundation for Young Scientists of China (No. 41802044) to W. Liang. Portions of this work were performed at GeoSoilEnviroCARS (the University of Chicago, Sector 13), Advanced Photon Source (APS), Argonne National Laboratory. GeoSoilEnviroCARS is supported by the National Science Foundation-Earth Sciences (No. EAR-1634415) and Department of Energy-GeoSciences (No. DE-FG02-94ER14466). 13-BM-C and GSECARS/COMPRES gas loading system are support in part by COMPRES under NSF Cooperative Agreement EAR-1661511. This research used resources of the Advanced Photon Source, a U.S. Department of Energy (DOE) Office of Science User Facility operated for the DOE Office of Science by Argonne National Laboratory under Contract No. DE-AC02-06CH11357. We thank the two anonymous reviewers for their constructive comments. The final publication is available at Springer via <https://doi.org/10.1007/s12583-021-1495-y>.

Electronic Supplementary Materials: Supplementary materials (Figures S1–S6; Supplementary Material A) are available in the online version of this article at <https://doi.org/10.1007/s12583-021-1495-y>.

Conflict of Interest

The authors declare that they have no conflict of interest.

REFERENCES CITED

- Angel, R. J., 2000. Equations of State. *Reviews in Mineralogy and Geochemistry*, 41(1): 35–59. <https://doi.org/10.2138/rmg.2000.41.2>
- Birch, F., 1978. Finite Strain Isotherm and Velocities for Single-Crystal and Polycrystalline NaCl at High Pressures and 300° K. *Journal of Geophysical Research: Solid Earth*, 83(B3): 1257–1268. <https://doi.org/10.1029/jb083ib03p01257>
- Boulard, E., Gloter, A., Corgne, A., et al., 2011. New Host for Carbon in the Deep Earth. *Proceedings of the National Academy of Sciences of the United States of America*, 108(13): 5184–5187. <https://doi.org/10.1073/pnas.1016934108>
- Boulard, E., Menguy, N., Auzende, A. L., et al., 2012. Experimental Investigation of the Stability of Fe-Rich Carbonates in the Lower Mantle. *Journal of Geophysical Research: Solid Earth*, 117(B2): B02208. <https://doi.org/10.1029/2011jb008733>
- Cerantola, V., Bykova, E., Kuppenko, I., et al., 2017. Stability of Iron-Bearing Carbonates in the Deep Earth's Interior. *Nature Communications*, 8: 15960. <https://doi.org/10.1038/ncomms15960>
- Cerantola, V., McCammon, C., Kuppenko, I., et al., 2015. High-Pressure Spectroscopic Study of Siderite (FeCO_3) with a Focus on Spin Crossover. *American Mineralogist*, 100(11/12): 2670–2681. <https://doi.org/10.2138/am-2015-5319>
- Chao, K. H., Hsieh, W. P., 2019. Thermal Conductivity Anomaly in ($\text{Fe}_{0.78}\text{Mg}_{0.22}\text{CO}_3$) Siderite across Spin Transition of Iron. *Journal of Geophysical Research: Solid Earth*, 124(2): 1388–1396. <https://doi.org/10.1029/2018jb017003>
- Chariton, S., McCammon, C., Vasiukov, D. M., et al., 2020. Seismic Detectability of Carbonates in the Deep Earth: A Nuclear Inelastic Scattering Study. *American Mineralogist*, 105(3): 325–332. <https://doi.org/10.2138/am-2020-6901>
- Dasgupta, R., Hirschmann, M. M., 2006. Melting in the Earth's Deep Upper Mantle Caused by Carbon Dioxide. *Nature*, 440(7084): 659–662. <https://doi.org/10.1038/nature04612>
- Dasgupta, R., Hirschmann, M. M., Withers, A. C., 2004. Deep Global Cycling of Carbon Constrained by the Solidus of Anhydrous, Carbonated Eclogite under Upper Mantle Conditions. *Earth and Planetary Science Letters*, 227(1/2): 73–85. <https://doi.org/10.1016/j.epsl.2004.08.004>
- Dziewonski, A. M., Anderson, D. L., 1981. Preliminary Reference Earth Model. *Physics of the Earth and Planetary Interiors*, 25(4): 297–356. [https://doi.org/10.1016/0031-9201\(81\)90046-7](https://doi.org/10.1016/0031-9201(81)90046-7)
- Farfan, G., Wang, S., Ma, H., et al., 2012. Bonding and Structural Changes in Siderite at High Pressure. *American Mineralogist*, 97(8/9): 1421–1426. <https://doi.org/10.2138/am.2012.4001>
- Farsang, S., Faq, S., Redfern, S. A. T., 2018. Raman Modes of Carbonate Minerals as Pressure and Temperature Gauges up to 6 GPa and 500 °C. *The American Mineralogist*, 103(11/12): 1988–1998
- Fei, Y. W., Zhang, L., Corgne, A., et al., 2007. Spin Transition and Equations of State of (Mg, FeO) Solid Solutions. *Geophysical Research Letters*, 34(17): L17307. <https://doi.org/10.1029/2007gl030712>
- Fiquet, G., Guyot, F., Kunz, M., et al., 2002. Structural Refinements of Magnesite at very High Pressure. *American Mineralogist*, 87(8/9): 1261–1265. <https://doi.org/10.2138/am-2002-8-927>
- Hazen, R. M., Prewitt, C. T., 1988. Effects of Temperature and Pressure on Interatomic Distances in Oxygen-Based Minerals. *Elastic Properties and Equations of State*. American Geophysical Union, Washington, D. C. <https://doi.org/10.1029/sp026p0407>
- Hsu, H., Huang, S. C., 2016. Spin Crossover and Hyperfine Interactions of Iron in (Mg, FeCO_3) Ferromagnesite. *Physical Review B*, 94(6): 060404. <https://doi.org/10.1103/physrevb.94.060404>
- Isshiki, M., Irifune, T., Hirose, K., et al., 2004. Stability of Magnesite and Its High-Pressure Form in the Lowermost Mantle. *Nature*, 427(6969): 60–63. <https://doi.org/10.1038/nature02181>
- Langille, D. B., O'Shea, D. C., 1977. Raman Spectroscopy Studies of Antiferromagnetic FeCO_3 and Related Carbonates. *Journal of Physics and Chemistry of Solids*, 38(10): 1161–1171. [https://doi.org/10.1016/0022-3697\(77\)90044-0](https://doi.org/10.1016/0022-3697(77)90044-0)
- Lavina, B., Dera, P., Downs, R. T., et al., 2009. Siderite at Lower Mantle Conditions and the Effects of the Pressure-Induced Spin-Pairing Transition. *Geophysical Research Letters*, 36(23): L23306. <https://doi.org/10.1029/2009gl039652>
- Lavina, B., Dera, P., Downs, R. T., et al., 2010a. Effect of Dilution on the Spin Pairing Transition in Rhombohedral Carbonates. *High Pressure Research*, 30(2): 224–229. <https://doi.org/10.1080/08957959.2010.485391>
- Lavina, B., Dera, P., Downs, R. T., et al., 2010b. Structure of Siderite FeCO_3 to 56 GPa and Hysteresis of Its Spin-Pairing Transition. *Physical Review B*, 82(6): 064110. <https://doi.org/10.1103/physrevb.82.064110>
- Lee, K. K. M., O'Neill, B., Panero, W. R., et al., 2004. Equations of State of the High-Pressure Phases of a Natural Peridotite and Implications for

- the Earth's Lower Mantle. *Earth and Planetary Science Letters*, 223(3/4): 381–393. <https://doi.org/10.1016/j.epsl.2004.04.033>
- Liang, W., Li, Z. M., Yin, Y., et al., 2018a. Single Crystal Growth, Characterization and High-Pressure Raman Spectroscopy of Impurity-Free Magnesite (MgCO_3). *Physics and Chemistry of Minerals*, 45(5): 423–434. <https://doi.org/10.1007/s00269-017-0930-1>
- Liang, W., Yin, Y., Li, Z. M., et al., 2018b. Single Crystal Growth, Crystalline Structure Investigation and High-Pressure Behavior of Impurity-Free Siderite (FeCO_3). *Physics and Chemistry of Minerals*, 45(9): 831–842. <https://doi.org/10.1007/s00269-018-0965-y>
- Lin, J. F., Liu, J., Jacobs, C., et al., 2012. Vibrational and Elastic Properties of Ferromagnesite across the Electronic Spin-Pairing Transition of Iron. *American Mineralogist*, 97(4): 583–591. <https://doi.org/10.2138/am.2012.3961>
- Litasov, K. D., Fei, Y. W., Ohtani, E., et al., 2008. Thermal Equation of State of Magnesite to 32 GPa and 2 073 K. *Physics of the Earth and Planetary Interiors*, 168(3/4): 191–203. <https://doi.org/10.1016/j.pepi.2008.06.018>
- Liu, J. C., Fu, S. Y., Lin, J. F., 2020. Spin Transition of Iron in Deep-Mantle Ferromagnesite. In: Manning, C. E., Lin J. F., Mao, W. L., eds., Carbon in Earth's Interior. American Geophysical Union, Washington D. C. <https://doi.org/10.1002/9781119508229.ch12>
- Liu, J., Lin, J. F., Mao, Z., et al., 2014. Thermal Equation of State and Spin Transition of Magnesiosiderite at High Pressure and Temperature. *American Mineralogist*, 99(1): 84–93. <https://doi.org/10.2138/am.2014.4553>
- Lobanov, S. S., Goncharov, A. F., 2020. Pressure-Induced $\text{Sp}^2\text{-Sp}^3$ Transitions in Carbon-Bearing Phases. In: Manning, C. E., Lin J. F., Mao, W. L., eds., Carbon in Earth's Interior, John Wiley & Sons, Hoboken. <https://doi.org/10.1002/9781119508229.ch1>
- Lobanov, S. S., Goncharov, A. F., Litasov, K. D., 2015. Optical Properties of Siderite (FeCO_3) across the Spin Transition: Crossover to Iron-Rich Carbonates in the Lower Mantle. *American Mineralogist*, 100(5/6): 1059–1064. <https://doi.org/10.2138/am-2015-5053>
- Lobanov, S. S., Holtgrewe, N., Goncharov, A. F., 2016. Reduced Radiative Conductivity of Low Spin FeO_6 -Octahedra in FeCO_3 at High Pressure and Temperature. *Earth and Planetary Science Letters*, 449: 20–25. <https://doi.org/10.1016/j.epsl.2016.05.028>
- Mattila, A., Pykkänen, T., Rueff, J. P., et al., 2007. Pressure Induced Magnetic Transition in Siderite FeCO_3 Studied by X-Ray Emission Spectroscopy. *Journal of Physics: Condensed Matter*, 19(38): 386206. <https://doi.org/10.1088/0953-8984/19/38/386206>
- McDonough, W. F., Sun, S. S., 1995. The Composition of the Earth. *Chemical Geology*, 120(3/4): 223–253. [https://doi.org/10.1016/0009-2541\(94\)00140-4](https://doi.org/10.1016/0009-2541(94)00140-4)
- Merlini, M., Hanfland, M., Salamat, A., et al., 2015. The Crystal Structures of $\text{Mg}_2\text{Fe}_2\text{C}_4\text{O}_{13}$, with Tetrahedrally Coordinated Carbon, and $\text{Fe}_{13}\text{O}_{19}$, Synthesized at Deep Mantle Conditions. *American Mineralogist*, 100(8/9): 2001–2004. <https://doi.org/10.2138/am-2015-5369>
- Merlini, M., Sapelli, F., Fumagalli, P., et al., 2016. High-Temperature and High-Pressure Behavior of Carbonates in the Ternary Diagram $\text{CaCO}_3\text{-MgCO}_3\text{-FeCO}_3$. *American Mineralogist*, 101(6): 1423–1430. <https://doi.org/10.2138/am-2016-5458>
- Müller, J., Speziale, S., Efthimiopoulos, I., et al., 2016. Raman Spectroscopy of Siderite at High Pressure: Evidence for a Sharp Spin Transition. *American Mineralogist*, 101(12): 2638–2644. <https://doi.org/10.2138/am-2016-5708>
- Nagai, T., Ishido, T., Seto, Y., et al., 2010. Pressure-Induced Spin Transition in FeCO_3 -Siderite Studied by X-Ray Diffraction Measurements. *Journal of Physics: Conference Series*, 215: 012002. <https://doi.org/10.1088/1742-6596/215/1/012002>
- Palyanov, Y. N., Bataleva, Y. V., Sokol, A. G., et al., 2013. Mantle-Slab Interaction and Redox Mechanism of Diamond Formation. *Proceedings of the National Academy of Sciences of the United States of America*, 110(51): 20408–20413. <https://doi.org/10.1073/pnas.1313340110>
- Ricolleau, A., Perrillat, J. P., Fiquet, G., et al., 2010. Phase Relations and Equation of State of a Natural MORB: Implications for the Density Profile of Subducted Oceanic Crust in the Earth's Lower Mantle. *Journal of Geophysical Research: Solid Earth*, 115(B8): 08202. <https://doi.org/10.1029/2009jb006709>
- Rividi, N., van Zuilen, M., Philippot, P., et al., 2010. Calibration of Carbonate Composition Using Micro-Raman Analysis: Application to Planetary Surface Exploration. *Astrobiology*, 10(3): 293–309. <https://doi.org/10.1089/ast.2009.0388>
- Robie, R. A., Haselton, H. T., Hemingway, B. S., 1984. Heat Capacities and Entropies of Rhodochrosite (MnCO_3) and Siderite (FeCO_3) between 5 and 600 K. *American Mineralogist*, 69: 349–357
- Rutt, H. N., Nicola, J. H., 1974. Raman Spectra of Carbonates of Calcite Structure. *Journal of Physics C: Solid State Physics*, 7(24): 4522–4528. <https://doi.org/10.1088/0022-3719/7/24/015>
- Sanchez-Valle, C., Ghosh, S., Rosa, A. D., 2011. Sound Velocities of Ferromagnesian Carbonates and the Seismic Detection of Carbonates in Eclogites and the Mantle. *Geophysical Research Letters*, 38(24): L24315. <https://doi.org/10.1029/2011gl049981>
- Santillan, J., 2005. An Infrared Study of Carbon-Oxygen Bonding in Magnesite to 60 GPa. *American Mineralogist*, 90(10): 1669–1673. <https://doi.org/10.2138/am.2005.1703>
- Sawchuk, K., Kamat, R., McGuire, C., et al., 2021. An X-Ray Diffraction and Raman Spectroscopic Study of the High-Pressure Behavior of Gaspéite ($\text{Ni}_{0.73}\text{Mg}_{0.27}\text{CO}_3$). *Physics and Chemistry of Minerals*, 48(1): 1–10. <https://doi.org/10.1007/s00269-020-01133-3>
- Shen, G. Y., Wang, Y. B., Dewaele, A., et al., 2020. Toward an International Practical Pressure Scale: A Proposal for an IPPS Ruby Gauge (IPPS-Ruby2020). *High Pressure Research*, 40(3): 299–314. <https://doi.org/10.1080/08957959.2020.1791107>
- Spivak, A., Solopova, N., Cerantola, V., et al., 2014. Raman Study of $\text{MgCO}_3\text{-FeCO}_3$ Carbonate Solid Solution at High Pressures up to 55 GPa. *Physics and Chemistry of Minerals*, 41(8): 633–638. <https://doi.org/10.1007/s00269-014-0676-y>
- Syracuse, E. M., van Keken, P. E., Abers, G. A., 2010. The Global Range of Subduction Zone Thermal Models. *Physics of the Earth and Planetary Interiors*, 183(1/2): 73–90. <https://doi.org/10.1016/j.pepi.2010.02.004>
- Taran, M. N., Müller, J., Friedrich, A., et al., 2017. High-Pressure Optical Spectroscopy Study of Natural Siderite. *Physics and Chemistry of Minerals*, 44(8): 537–546. <https://doi.org/10.1007/s00269-017-0880-7>
- Weis, C., Sternemann, C., Cerantola, V., et al., 2017. Pressure Driven Spin Transition in Siderite and Magnesiosiderite Single Crystals. *Scientific Reports*, 7: 16526. <https://doi.org/10.1038/s41598-017-16733-3>
- Williams, Q., Collerson, B., Knittle, E., 1992. Vibrational Spectra of Magnesite (MgCO_3) and Calcite-III at High Pressures. *American Mineralogist*, 77: 1158–1165. <https://doi.org/10.1180/minmag.1992.056.385.19>
- Yao, X., Xie, C. W., Dong, X. A., et al., 2018. Novel High-Pressure Calcium Carbonates. *Physical Review B*, 98: 014108. <https://doi.org/10.1103/physrevb.98.014108>

- Ye, Y., Prakapenka, V., Meng, Y., et al., 2017. Intercomparison of the Gold, Platinum, and MgO Pressure Scales up to 140 GPa and 2 500 K. *Journal of Geophysical Research: Solid Earth*, 122(5): 3450–3464. <https://doi.org/10.1002/2016jb013811>
- Ye, Y., Shim, S. H., Prakapenka, V., et al., 2018. Equation of State of Solid Ne Inter-Calibrated with the MgO, Au, Pt, NaCl-B2, and Ruby Pressure Scales up to 130 GPa. *High Pressure Research*, 38(4): 377–395. <https://doi.org/10.1080/08957959.2018.1493477>
- Zhang, J. Z., Martinez, I., Guyot, F., et al., 1998. Effects of Mg-Fe (Super 2+) Substitution in Calcite-Structure Carbonates, Thermoelastic Properties. *American Mineralogist*, 83(3/4): 280–287. <https://doi.org/10.2138/am-1998-3-411>
- Zhang, J., Martinez, I., Guyot, F., et al., 1997. X-Ray Diffraction Study of Magnesite at High Pressure and High Temperature. *Physics and Chemistry of Minerals*, 24(2): 122–130. <https://doi.org/10.1007/s002690050025>